

The Origin of Solar Filament Plasma Inferred from in situ Observations of Elemental Abundances

H.Q. SONG^{1,2}, Y. CHEN¹, B. LI¹, L.P. LI², L. ZHAO³, J.S. HE⁴, D. DUAN⁴, X. CHENG⁵, AND J. ZHANG⁶

1 Shandong Provincial Key Laboratory of Optical Astronomy and Solar-Terrestrial Environment, and Institute of Space Sciences, Shandong University, Weihai, Shandong 264209, China

`hqsong@sdu.edu.cn`

2 Key Laboratory of Solar Activity, National Astronomical Observatories, Chinese Academy of Sciences, Beijing 100012, China

3 Department of Climate and Space sciences and Engineering, University of Michigan, Ann Arbor, MI 48105, USA

4 School of Earth and Space Sciences, Peking University, Beijing 100871, China

5 School of Astronomy and Space Science, Nanjing University, Nanjing, Jiangsu 210093, China

6 Department of Physics and Astronomy, George Mason University, Fairfax, VA 22030, USA

ABSTRACT

Solar filaments/prominences are one of the most common features in the corona, which may lead to energetic coronal mass ejections (CMEs) and flares when they erupt. Filaments are about one hundred times cooler and denser than the coronal material, and physical understanding of their material origin remains controversial. Two types of scenarios have been proposed: one argues that the filament plasma is brought into the corona from photosphere or chromosphere through a siphon or evaporation/injection process, while the other suggests that the material condenses from the surrounding coronal plasma due to thermal instability. The elemental abundance analysis is a reasonable clue to constrain the models, as the siphon or evaporation/injection model would predict that the filament material abundances are close to the photospheric or chromospheric ones, while the condensation model should have coronal abundances. In this letter, we analyze the elemental abundances of a magnetic cloud that contains the ejected filament material. The corresponding filament eruption occurred on 1998 April 29, accompanying an M6.8 class soft X-ray flare located at the heliographic coordinates S18E20 (NOAA 08210) and a fast halo CME with the linear velocity of 1374 km s^{-1} near the Sun. We find that the abundance ratios of elements with low and high First

Ionization Potential such as Fe/O, Mg/O, and Si/O are 0.150, 0.050, and 0.070, respectively, approaching their corresponding photospheric values 0.065, 0.081, and 0.066, which does not support the coronal origin of the filament plasma.

Subject headings: Sun: filaments, prominences – Sun: abundances – Sun: coronal mass ejections (CMEs)

1. INTRODUCTION

Solar filaments, also known as prominences when observed on the solar limb, are one of the most common features in the corona. It has been found that over 70% of coronal mass ejections (CMEs) are associated with filament eruptions (e.g., Webb & Hundhausen 1987; Gopalswamy et al. 2003). The associated CMEs usually exhibit typical three-part structures, *i.e.*, the bright leading front, the dark cavity, and the bright core that is believed to correspond with the filament (House et al. 1981). Filaments are about one hundred times cooler ($T \sim 10^4$ K) and denser than the coronal material ($T \sim 10^6$ K). Two crucial issues need to be addressed to understand the filament formation (e.g., Parenti 2014; Li & Zhang 2013; Zhou et al. 2014): what is their magnetic structure (Yan et al. 2015, 2016) and where does their material come from (Spicer et al. 1998; Mackay et al. 2010)? Our understanding on the origin of the filament material remains controversial. Two types of explanations have been proposed: one argues that the filament plasma is brought into the corona from photosphere and/or chromosphere. For instance, a siphon effect can bring material into the corona from the photosphere or chromosphere (e.g., Spicer et al. 1998), and the chromospheric plasma can enter into the corona through evaporation or injection process (Mackay et al. 2010; Parenti 2014); the other one suggests that the surrounding coronal material condenses and forms the filament due to thermal instability (e.g., Sakai et al. 1987; Démoulin, 1993).

The elemental abundance measurement is a reasonable method to constrain the models, because the coronal abundances are known to differ from those of photosphere due to the first ionization potential (FIP) effect (Schmelz et al. 2012; Laming 2015). Usually, the abundance ratios of elements with low FIP (<10 eV, *e.g.*, iron, magnesium, and silicon) and those with high FIP (>10 eV, *e.g.*, oxygen and neon) will be enhanced in the corona, which is supported by the spectroscopic and solar wind data (e.g., Schmelz et al. 2012 and references therein). For example, it is generally accepted that magnetic flux ropes (MFRs) form in the corona, therefore large FIP fractionations are frequently associated with magnetic clouds (MCs, Zurbuchen et al. 2004; Smith et al. 2001). This elemental fractionation results from a separation of ions and neutrals, taking place between the photosphere and corona. The siphon and evaporation/injection model would predict that the filament material abundances are close to the photospheric or chromospheric ones, while the condensation model should have coronal abundances. Some abundance analyses through spectroscopy have been conducted to address this issue (Widing et al. 1986; Spicer et al. 1998). Their results showed that the magnesium-to-neon ratios have values intermediate between the photosphere and

corona but none are as high as expected in the corona. This indicates the filament material should not originate from the corona (Spicer et al. 1998).

Spectroscopy method has been pretty good and widely used to determine the abundances of astrophysical objects, while the method has a particular problem for the filament analysis because of its optical thickness. The radiation transfer process will hinder us to infer the precise elemental abundances of its interior. Therefore, it is still an open question about the origin of filament material. An alternative method to address this issue is to measure the filament abundances in the interplanetary space, which requires a clear identification of the filament material with in situ data. The filament is cooler in the corona as mentioned, so filament plasma will yield a significant fraction of ions with low-ionization temperatures, *e.g.*, Fe^{6+} , instead of Fe^{10+} in background solar wind or Fe^{16+} in hot regions within ICMEs (Song et al. 2016). This can be used to identify the filament in the interplanetary space (Lepri & Zurbuchen, 2010).

As mentioned, over 70% of CMEs are associated with filament eruptions. However, only $\sim 4\%$ of detected ICMEs have significant contributions of ions with low charge states ($\text{Fe}^{4+} \sim \text{Fe}^{7+}$), *i.e.*, exhibiting the signature of filaments (Lepri & Zurbuchen 2010), and usually their filament durations last only 1 to several hours (Yao et al. 2010), too short for the elemental abundance analysis as the temporal resolution is 2 hours. In an earlier statistical study (Song et al. 2016), we found a filament eruption event on 1998 April 29 that had a long (~ 20 hours) duration when propagating to the L1 point. Gloeckler et al. (1999) found anomalously large enrichment of ${}^3\text{He}^{++}/{}^4\text{He}^{++}$, He/O and Fe/O in this event. Skoug et al. (1999) reported that there existed a prolonged He^+ enhancement within this ICME, indicating the prominence material. However, neither of them paid attention to the origin of filament plasma. In this letter, we revisit this event to address this issue through investigating the filament elemental abundances. *Advanced Composition Explorer (ACE)* provides both the Fe charge state and elemental abundance information, which is used to identify the filament material and infer its origin. The proton velocity distribution functions (VDFs, Marsch et al. 1982; He et al. 2015) inside the filament are also analyzed. We introduce the instruments and methods in Section 2 and present the observational results in Section 3. Our summary and discussion is presented in the final Section.

2. INSTRUMENTS AND METHODS

The eruption process is recorded by the Extreme Ultraviolet Telescope (EIT, Delaboudiniere et al. 1995) 195 Å passband and Large Angle and Spectrometric Coronagraph (LASCO, Brueckner et al. 1995) on board the *Solar and Heliosphere Observatory (SOHO)*. With the EIT 304 Å data, we identify that this event was associated with a filament eruption. The soft X-ray (SXR) data are from the *Geostationary Operational Environment Satellite (GOES)*, which provides the integrated full-disk SXR emission from the Sun.

The *in situ* ion-charge states and elemental abundances are from the Solar Wind Ion Com-

position Spectrometer (SWICS, Gloeckler et al. 1998) on board the *ACE*, which was launched in 1997 and orbiting around the L1 point. As a mass spectrometer, SWICS consists of a time-of-flight system (TOF) and an energy resolving solid-state detector (SSD). Through measuring the speed of each ion and determining its residual energy with TOF and SSD, respectively, the mass, charge, and energy of each detected ion can be identified. SWICS can provide the charge-state distributions and abundances of ~ 10 elements (Lepri et al. 2001). Here the newly released SWICS 1.1 level 2 data are used (Shearer et al. 2014), which have a better accuracy than the earlier versions with improved calibration. The new version improved the process to remove accidental coincidence events, resulting in an increasing identification of rare ions (*e.g.*, Fe^{6+} and Fe^{7+}). This is crucial to identify the filament and to diagnose its abundances in the present study. We also use the magnetic field and plasma data from MAG (Smith et al. 1998) and SWEFAM (McComas et al. 1998) on board *ACE*. The proton three-dimensional (3D) VDFs within the ICME are measured by 3DP (Lin et al. 1995) onboard *WIND*. Here we adopt a tri-quadratic interpolation method (Marsch et al. 1982; He et al. 2015) to reconstruct the full 3D VDF from the 3DP data.

3. OBSERVATIONS AND RESULTS

3.1. Overview of the Eruption

An M6.8 class SXR flare, located at the heliographic coordinates S18E20 (NOAA 08210) from the Earth perspective, was recorded by *GOES* on 1998 April 29. The corresponding SXR flux rose from $\sim 16:06$ UT and peaked at $\sim 16:37$ UT as shown in Figure 1(a). The eruption process was observed by the EIT 195 Å (~ 1.5 MK) passband as exhibited with the animation available online. We present its post-eruptive arcades (PEAs, Tripathi et al. 2004) in Figure 1(b), and the associated CME recorded by the LASCO C3 with field of view (FOV) of 4–18 R_{\odot} in Figure 1(c). The CME was a halo one due to its propagation toward the Earth with a linear velocity of 1374 km s^{-1} in the LASCO FOV (<https://cdaw.gsfc.nasa.gov/>). To make sure that this is a filament eruption event, we checked the EIT 304 Å (~ 0.06 MK) images, which are suitable to identify the cooler filament. There were only two frames on 1998 April 29 for EIT 304 Å. Fortunately, these two frames were taken before and after the eruption respectively and confirmed that the event was a filament eruption (see Figures 1(d) and (e)). The green arrows and the dotted line in Figure 1(d) depict the filament prior to the eruption. In Figure 1(e), the filament was invisible due to its full eruption.

According to the online ICME list (<http://www.srl.caltech.edu/ACE/ASC/DATA/level3/icmetable2.htm>) compiled by Richardson and Cane (Cane & Richardson, 2003; Richardson & Cane, 2010), the shock generated by this ICME arrived at *ACE* on 1998 May 1. We also evaluate the arrival time with the shock propagation model (SPM, Feng & Zhao, 2006; Zhao & Feng 2014), which is based on an analytic solution of blast wave to predict the interplanetary shock arrival times. Here the SPM model predicts that

the shock should arrive around 21:00 UT on 1998 May 1, very close to the observed moment at 21:21 UT as shown in Figure 2. Therefore, there is no doubt that the ICME detected by *ACE* corresponds to the halo CME associated with the filament eruption.

3.2. The Filament Plasma and Elemental Abundance Analysis

In 1998 May, both *ACE* and *WIND* orbited around the L1 point, and the distance between them can be neglected compared with the much larger ICME scale (see e.g., Song et al. 2016). We demonstrate this point in Figures 2(a) and (b), which show the magnetic field measured by *ACE* and *WIND*, respectively. The total magnetic field strength is presented with black lines and its three components are plotted in the Geocentric Solar Ecliptic coordinate. The X-axis (red) points from the Earth toward the Sun, the Y-axis (green) points toward the opposite direction of the Earth’s motion, and the Z-axis (blue) is parallel to the ecliptic pole. It is obvious that the magnetic field profiles in these two panels are almost identical, proving that both spacecraft passed through the same part of the ICME structure. The shock, pointed out with the purple vertical solid line, arrived at 21:21 UT on May 1, and the magnetic cloud (MC), exhibiting low thermal velocities of protons, started from 11:31 UT on May 2 and ceased until 16:48 UT on May 3. The MC boundaries are marked with two purple vertical dot-dashed lines.

Figure 2(c) is the normalized pitch angle distribution (PAD) of 272 eV electrons measured by *ACE*, exhibiting bidirectional electrons (BDEs) during the MC passage as expected if the MFR two footpoints keep anchored on the Sun during the propagation. The velocity profile within the MC decreases, from 650 to 430 km s⁻¹, with time as shown in Figure 3(d), indicating the expansion of the MFR. Figure 3(e) presents the thermal velocity (red) and number density (black) of protons. One of the typical MC characteristics, *i.e.*, lower temperature, is demonstrated clearly with the red solid line. The thermal velocity within MC (~ 15 km s⁻¹) corresponds to $\sim 10^4$ K. While one interesting phenomenon is that there exists an extended region of high density, over 30 cm⁻³ in general, as emphasized with yellow shade, corresponding to the presumed filament material. The dynamical and total perpendicular pressures are plotted in Figure 2(f) with red and black lines, respectively, showing that the pressure within the shade considerably larger than those of the other regions. Correspondingly, the plasma β (red line in Figure 2(g)) within the shade is greatly enhanced reaching an maximum of 10, due to the high density there. This is not the typical MC characteristics (Burlaga et al. 1981). The black line in Figure 2(g) demonstrates that the entropy of the shaded region is lower than that of the other regions. Note Figures 2(e)–(g) are provided by *WIND* as *ACE* does not have the corresponding data within the shade.

The Fe charge state distributions with a temporal resolution of 2 h, ranging between 6+ and 20+, in Figure 2(h) show that large amount of low ionization states such as 6+ and 7+ exists in the yellow shade. Correspondingly, the average iron charge state ($\langle Q \rangle_{\text{Fe}}$) decreased from over 16+ to near 6+ as demonstrated with the white solid line, which is obviously lower than those of the solar wind ($\sim 9+$ to 11+). Note the white horizontal dotted line represents the position of 9+.

All of the observed features, including the low temperature, high density, and low Fe charge states, are consistent with the filament characteristics, providing strong evidence that the shaded region is the interplanetary counterpart of the erupted filament as presented in Figure 1 (see also Lepri & Zurbuchen, 2010).

Figure 3 shows the elemental abundances to infer the origin of the filament material with SWICS. The Fe charge state distributions are re-plotted in Figure 3(a) to identify the filament interval. For comparison, two regions with Fe charge states higher and lower than those in the normal solar wind are emphasized with yellow shades, which are the non-filament (left) and filament (right) intervals within the ICME, respectively. Note that to represent the filament, we select a shorter region in Figure 3 (in comparison with Figure 2) with dominated lower Fe charge states ($\langle Q \rangle_{\text{Fe}} < 9+$).

As mentioned, the abundance ratios of elements with low and high FIP (e.g., Fe/O, Mg/O, and Si/O) will be enhanced in the corona, and large FIP fractionations are frequently associated with MCs as they form in the corona. The variations of abundance ratios within MCs indicate their plasmas should have different origins. Figures 3(b)-(d) show the Fe/O, Mg/O, and Si/O ratios sequentially with a temporal resolution of 2 h. The horizontal dotted lines in these panels depict the corresponding elemental ratios of the solar photosphere (Asplund et al. 2009). The ratios in the non-filament region are obviously different from those in the filament region. For instance, the Fe/O (Mg/O and Si/O) ratios in non-filament region are around 0.25 (0.30 and 0.30), while those in the filament region approach 0.150 (0.050 and 0.070), which are closer to the photospheric values of 0.065 (0.081 and 0.066). Therefore, our in situ observations do not support that the filament material originates from the corona.

3.3. The Velocity Distribution Functions within the Filament

Yao et al. (2010) presented in situ observations of three MCs that contain cold and high-density material at 0.3, 0.5, and 0.7 AU with *Helios 2*. They investigated the microstates of the filaments with the thermal proton VDFs, which were cooler compared to non-filament plasmas. But two filaments showed obvious anisotropic feature, and the other one was close to isotropic. It is likely that different features originated from different filaments. However, the intervals with filament in their events were very short (~ 1 h), so they did not examine whether the difference of VDFs exists within the same filament.

Here the interval of filament lasted about 20 h, allowing us to examine the VDFs at different locations with *WIND* measurements. Figure 4 illustrates the cross-section view of the VDFs from one orthogonal visual angle at different locations as marked with filled circles in Figures 2(e) and 3(a). The cut view here is defined by the coordinate axis pair $[R, (B_0 \times R) \times R]$, where R is the radial direction and B_0 is the local mean magnetic field vector. Figure 4(a) shows the non-filament region, and (b)-(d), the filament. It is obvious that the VDFs in (a) is larger compared to those presented

in other panels, which is consistent with their respective temperatures. The selected non-filament region approaches isotropic, yet different types of VDFs appear within the filament. Figure 4(b) exhibits an isotropic VDF, while (c) and (d) demonstrate a dominant heating perpendicular to the magnetic field indicated by the white solid line. Therefore, we confirm that both isotropic and anisotropic features can appear within the same one filament. However, it is not clear yet that the observed VDF difference originates in the solar atmosphere or is formed during the filament propagation in the interplanetary space.

4. SUMMARY AND DISCUSSION

In this letter, an erupted active-region filament, accompanied by an M6.8 class SXR flare and a halo CME with linear velocity of 1374 km s^{-1} near the Sun (<https://cdaw.gsfc.nasa.gov/>), was detected by both *ACE* and *WIND* at the L1 point, which was unambiguously proved by the high density, low temperature, and low Fe charge states in the interval. The elemental ratios with low and high FIP were deduced to infer the origin of filament material. The results show that the Fe/O (Mg/O and Si/O) ratios of non-filament interval are around 0.25 (0.30 and 0.30), while those of filament interval approach 0.150 (0.050 and 0.070), closer to the photospheric values of 0.065 (0.081 and 0.066). As this filament originated from an active region (NOAA 08210), and its origin may be different from that of quiescent filaments. Therefore, our in situ observations do not support that active-region filament plasma originates from the corona. The analysis of VDFs demonstrates that the same filament can exhibit both isotropic and anisotropic features near 1 AU.

As mentioned, only $\sim 4\%$ of detected ICMEs exhibit the signature of filaments and most of them have a short duration of 1 to several hours. This may be partially attributed to that the filament material only occupies a small fraction of ICME. The filament reported in this study is very special and prominent for its extended duration (~ 20 h). We use a velocity-modified Gold and Hoyle model to fit the MC (Gold & Hoyle, 1960; Wang et al. 2016), and find the spacecraft passed through the interior of the MC, close to the MC center. This may explain why the filament interval was so long. Nevertheless, this event offers us an excellent opportunity to investigate the elemental abundances of filament interior with in situ data.

Given that the FIP fractionation takes place between the photosphere and corona, the elemental abundances at different altitudes in the chromosphere are expected to vary between the photospheric and coronal values. Therefore, our analysis cannot definitively determine whether the filament plasma comes from the photosphere or chromosphere. Nonetheless, in agreement with Spicer et al. (1998), our study does not support the coronal origin of filament plasma.

As mentioned, large FIP fractionations (e.g., high Fe/O ratios) are frequently associated with MCs. However, within some MCs, there exist low Fe/O ratios close to the photospheric values without accompanying filament features (low Fe charge state and high proton density). These plasmas might correspond to the chromospheric ones that are evaporated into the corona along the

magnetic field lines stretched by the rising MFRs during the eruptions and then involved into the MFRs through magnetic reconnection. The evaporated plasmas during eruptions are hot with high charge states and low Fe/O ratios, which are different from the filament material with low charge states and low Fe/O ratios.

We are grateful to the referee, Drs. S.T. Lepri, Y.M. Wang, P.F. Chen, J. Lin, S. Yao, H. Tian, X.L. Yan, X.H. Zhao, G. Li, and Q. Hu for their valuable comments and discussion. We acknowledge the use of data from the *GOES*, *SOHO*, *ACE* and *WIND* missions. This work is supported by NSFC grants 41274177, 41274175, and 41331068. J.Z. is supported by US NSF AGS-1249270 and NSF AGS-1156120. L.Z. is supported by NSF grants AGS-1344835 and AGS-1621686. H.Q.S. is also supported by the open research program of CAS Key Laboratory of Solar Activity.

REFERENCES

- Asplund, M., Grevesse, N., Sauval, A.J., & Scott, P. 2009, *Annu. Rev. Astro. Astrophys.*, 47, 481
- Burlaga, L., Sittler, E., Mariani, F., & Schwenn, R. 1981, *J. Geophys. Res.*, 86, 6673
- Brueckner, G.E., Howard, R.A., Koomen, M.J., et al. 1995, *Sol. Phys.*, 162, 357
- Cane, H. V., & Richardson, I. G. 2003, *J. Geophys. Res.*, 108, SSH 6-1
- Delaboudiniere, J.P., Artzner, G.E., Brunaud, J., et al. 1995, *Sol. Phys.*, 162, 291
- Démoulin, P. 1993, *Advances in Space Research*, 13, 95
- Feng, X.S., & Zhao, X.H., 2006, *Sol. Phys.*, 238, 167
- Gloeckler, G., Cain, J., Ipavich, F. M., et al. 1998, *Space Sci. Rev.*, 86, 497
- Gold, T., & Hoyle, F. 1960, *Mon. Not. R. Astron. Soc.*, 120, 89
- Gopalswamy, N., Shimojo, M., Lu, W., et al. 2003, *ApJ*, 586, 562
- He, J.S., Wang, L.H., Tu, C.Y., et al. 2015, *ApJ*, 800, L31
- House, L.L., Wagner, W.J., Hildner, E., Sawyer, C., & Schmidt, H.U. 1981, *ApJ*, 244, L117
- Laming, J. M. 2015, *Living Reviews in Solar Physics*, 12, 2
- Lepri, S. T., Zurbuchen, T. H., Fisk, L. A., et al. 2001, *J. Geophys. Res.*, 106, 29231
- Lepri, S. T., & Zurbuchen, T. H. 2010, *ApJ*, 723, L22
- Li, L.P., & Zhang, J. 2013, *Sol. Phys.*, 282, 147

- Lin, R.P., Anderson, K.A. Ashford, S., et al. 1995, *Space Sci. Rev.*, 71, 125
- Mackay, D.H., Karpen, J.T., Ballester, J.L., et al. 2010, *Space Sci. Rev.*, 151, 333
- Marsch, E., Schwenn, R., Rosenbauer, R., et al. 1982, *J. Geophys. Res.*, 87, 52
- McComas, D. J., Bame, S. J., Barker, P., et al. 1998, *Space Sci. Rev.*, 86, 563
- Parenti, S. 2014, *Living Reviews in Solar Physics*, 11, 1
- Richardson, I. G., & Cane, H. V. 2010, *Sol. Phys.*, 264, 189
- Sakai, J., Colin, A., & Priest, E. 1987, *Sol. Phys.*, 114, 253
- Schmelz, J.T., Reames, D.V., von Steiger, R., & Basu, S. 2012, *ApJ*, 755, 33
- Shearer, P., von Steiger, R., Raines, J. M. et al. 2014, *ApJ*, 789, 60
- Smith, C. W., L’Heureux, J., Ness, N. F., et al. 1998, *Space Sci. Rev.*, 86, 613
- Smith, C. W., Ness, N. F., Burlaga, L. F., et al., 2001, *Sol. Phys.*, 204, 227
- Spicer, D.S., Feldman, U., Widing, K.G., & Rilee, M. 1998, *ApJ*, 494, 450
- Song, H.Q., Zhong, Z., Chen, Y., et al. 2016, *ApJS*, 224, 27
- Tripathi, D., Bothmer, V., & Cremades, H. 2004, *A&A*, 422, 337
- Wang, Y.M., Zhuang, B., Hu, Q., et al. 2016, *arXiv:1608.05607*.
- Webb, D.F., & Hundhausen, A.J. 1987, *Sol. Phys.*, 108, 383
- Widing, K.G., Feldman, U., & Bhatia, A.K. 1986, *ApJ*, 308, 982
- Yan, X.L., Priest, E.R., Guo, Q.L., et al. 2016, *ApJ*, 832, 23
- Yan, X.L., Xue, Z.K., Pan, G.M., et al. 2015, *ApJS*, 219, 17
- Yao, S. Marsch, E., Tu, C. Y., & Schwenn, R. 2010, *J. Geophys. Res.*, 115, A05103
- Zhao, X.H., & Feng, X.S., 2014, *J. Geophys. Res.*, 119, 1
- Zhou, Y.H., Chen, P.F., Zhang, Q.M., & Fang, C., 2014, *Research in Astronomy and Astrophysics*, 14, 581
- Zurbuchen, T. H., Gloeckler, G., Ipavich, F., et al. 2004, *Geophys. Res. Lett.*, 31, 11805

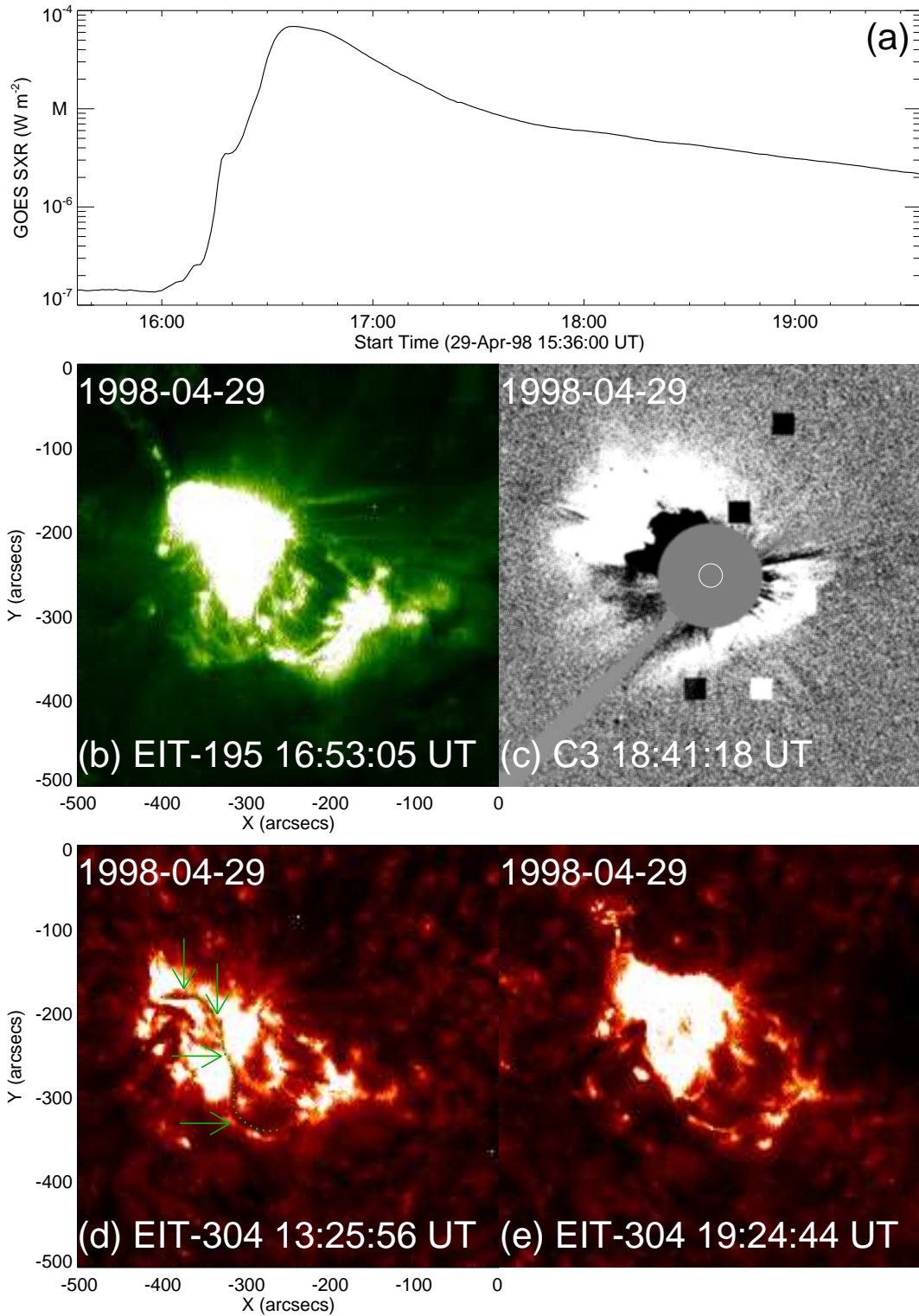


Fig. 1.— A filament eruption event on 1998 April 29. (a) The *GOES* SXR 1-8 Å flux profile of the accompanying flare. (b) EIT 195 Å (~ 1.5 MK) image after the eruption, showing the PEAs at high temperature. (c) The associated halo CME recorded by LASCO C3. (d)–(e) The EIT 304 Å (~ 0.06 MK) images, showing the low-temperature filament visible (prior to eruption) and invisible (after eruption), respectively. (An animation of this figure is available.)

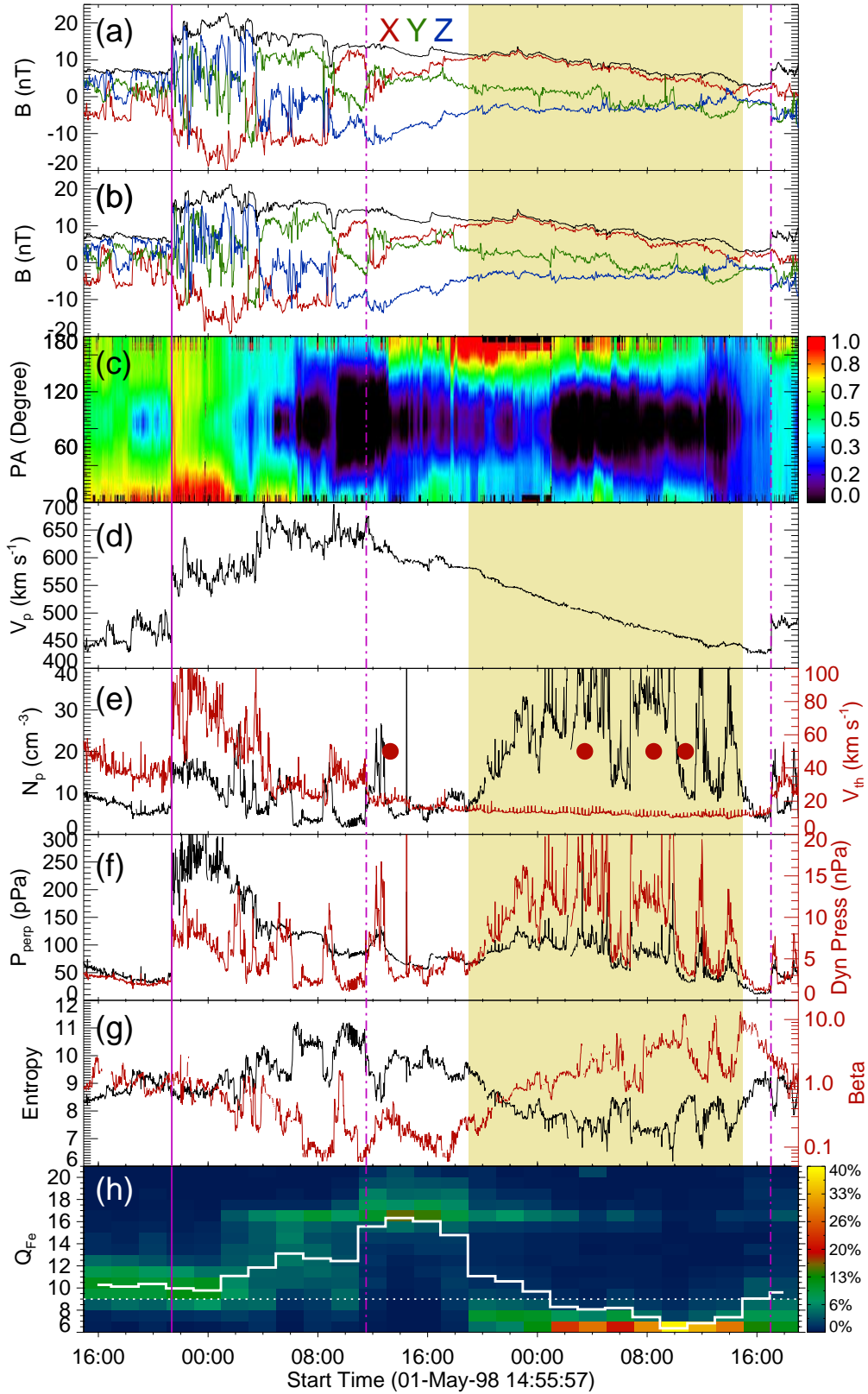


Fig. 2.— Plasma parameters measured with *ACE* and *WIND*. The panels show the total magnetic field strength (black) and its X (red), Y (green) and Z (blue) components from both *ACE* and *WIND* (a and b), PAD of electrons at 272 eV (c), bulk speed (d), thermal velocity (red) and density (black) (e), the dynamic pressure (red) and the total pressure along the perpendicular direction (black) (f), plasma β (red) and entropy (black) (g). Each energy state distribution map as

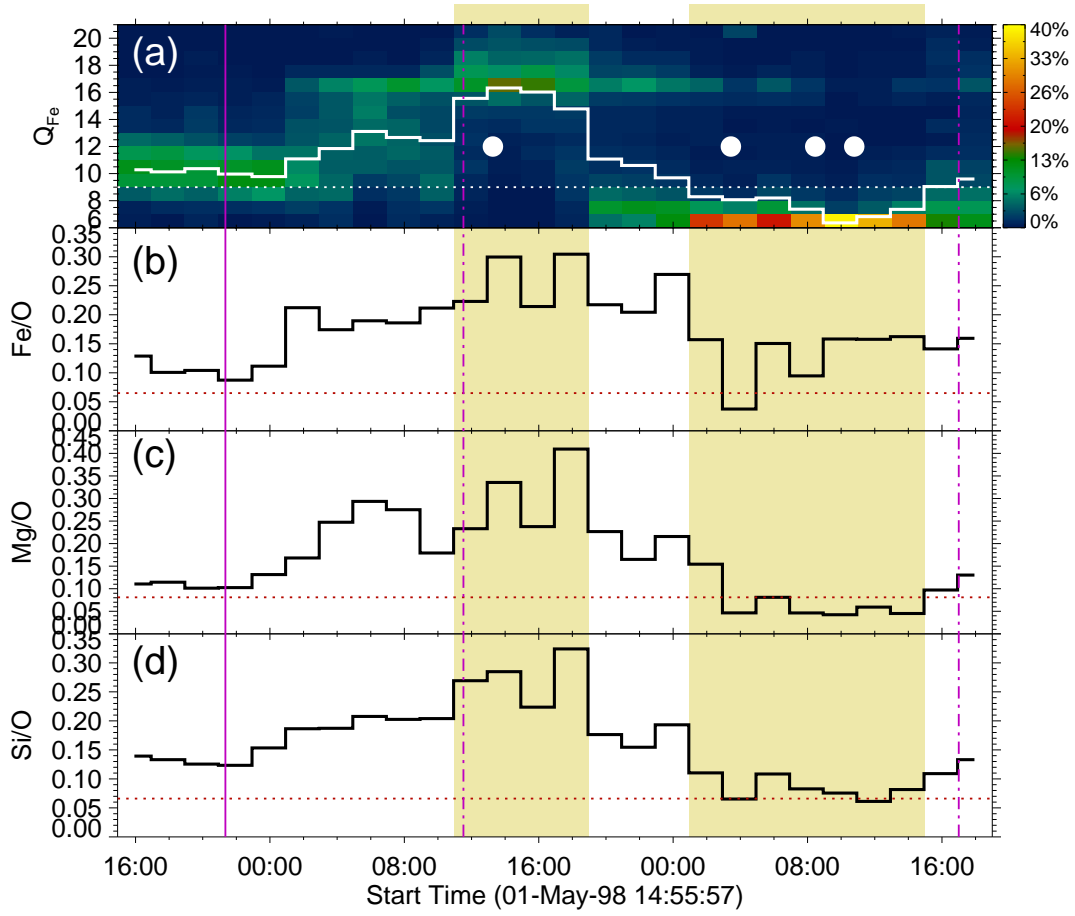


Fig. 3.— Charge states and elemental abundances measured with *ACE*. The panels show the Fe charge-state-distribution map and the $\langle Q \rangle_{\text{Fe}}$ profile (a), the temporal profiles of Fe/O (b), Mg/O (c), and Si/O (d). The red horizontal dotted lines in panels (b)-(d) shows the corresponding elemental ratios of the solar photosphere.

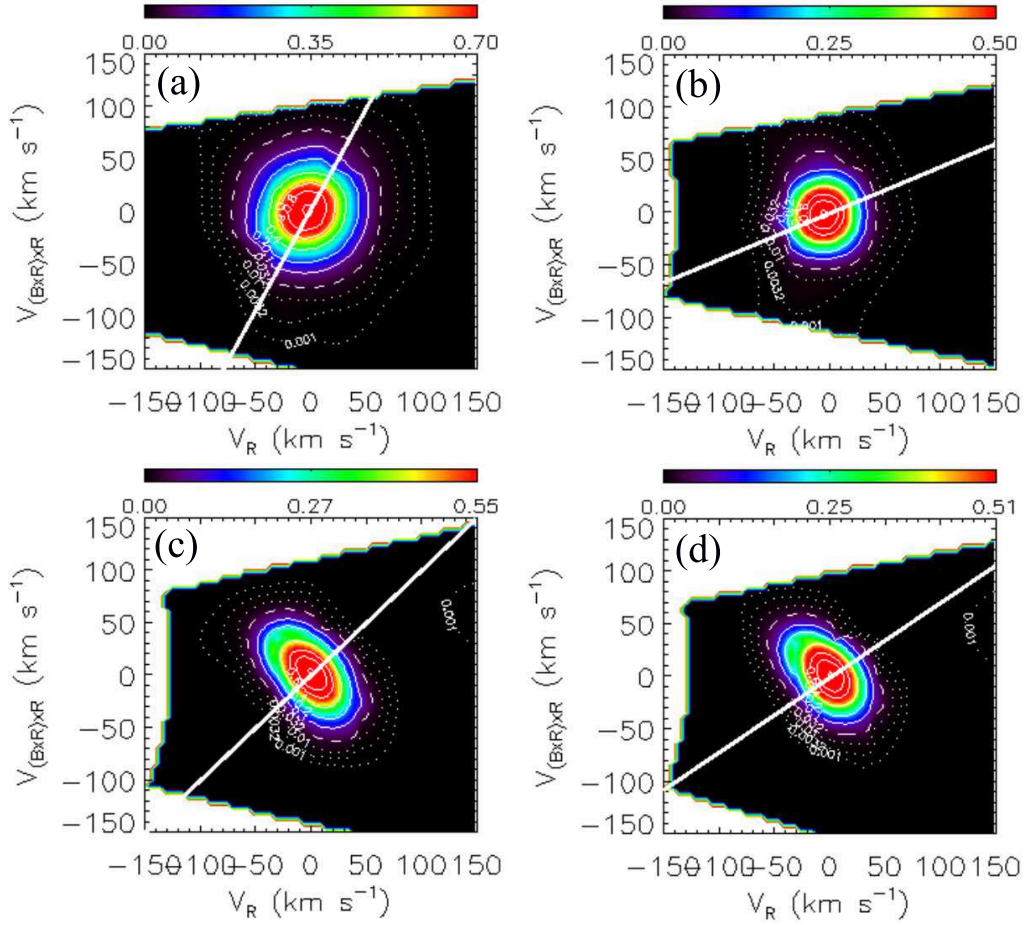


Fig. 4.— Cross sections of VDFs measured with *WIND*. Panels (a)-(d) correspond to the positions marked with four filled circles in Figures 2(e) and 3(a). The coordinate origin is set at the velocity of the maximum reduced-VDF values. The contours are 0.98, 0.8, 0.6, 0.4, 0.2, 0.1, 0.032, and 0.001 from inner to outer sequentially. The white solid line indicates the direction of background magnetic field.